

MJO Intensification with Warming in the Superparameterized CESM

NATHAN P. ARNOLD

Department of Earth and Planetary Sciences, Harvard University, Cambridge, Massachusetts

MARK BRANSON

Department of Atmospheric Science, Colorado State University, Fort Collins, Colorado

ZHIMING KUANG

Department of Earth and Planetary Sciences, and School of Engineering and Applied Sciences, Harvard University, Cambridge, Massachusetts

DAVID A. RANDALL

Department of Atmospheric Science, Colorado State University, Fort Collins, Colorado

ELI TZIPERMAN

Department of Earth and Planetary Sciences, and School of Engineering and Applied Sciences, Harvard University, Cambridge, Massachusetts

(Manuscript received 3 July 2014, in final form 12 November 2014)

ABSTRACT

The Madden–Julian oscillation (MJO) is the dominant mode of tropical intraseasonal variability, characterized by an eastward-propagating envelope of convective anomalies with a 30–70-day time scale. Here, the authors report changes in MJO activity across coupled simulations with a superparameterized version of the NCAR Community Earth System Model. They find that intraseasonal OLR variance nearly doubles between a preindustrial control run and a run with $4\times\text{CO}_2$. Intraseasonal precipitation increases at a rate of roughly 10% per 1 K of warming, and MJO events become 20%–30% more frequent. Moist static energy (MSE) budgets of composite MJO events are calculated for each scenario, and changes in budget terms are used to diagnose the physical processes responsible for changes in the MJO with warming. An increasingly positive contribution from vertical advection is identified as the most likely cause of the enhanced MJO activity. A decomposition links the changes in vertical advection to a steepening of the mean MSE profile, which is a robust thermodynamic consequence of warming. Surface latent heat flux anomalies are a significant sink of MJO MSE at $1\times\text{CO}_2$, but this damping effect is reduced in the $4\times\text{CO}_2$ case. This work has implications for organized tropical variability in past warm climates as well as future global warming scenarios.

1. Introduction

The Madden–Julian oscillation (MJO) consists of a broad envelope of enhanced convection that forms episodically over the Indian Ocean, propagates slowly eastward at around 5 m s^{-1} , and dissipates over the cooler waters of the central Pacific (Madden and Julian

1971; Zhang 2005). The convective signal is coupled to a large scale overturning circulation that suppresses deep convection in neighboring longitudes and closely resembles a forced Rossby–Kelvin response (Matthews et al. 2004; Gill 1980). In addition to its direct impact on tropical rainfall, the MJO is known to modulate the Asian, Australian, and West African monsoons (Pai et al. 2011; Lee et al. 2013; Lavender and Matthews 2009; Lawrence and Webster 2002; Hendon and Liebmann 1990); affect tropical cyclogenesis in both the Atlantic and Pacific basins (Hall et al. 2001; Maloney and Hartmann 2000; Liebmann et al. 1994; Frank and Roundy

Corresponding author address: Nathan Arnold, Colorado State University, 200 West Lake St., 1371 Campus Delivery, Fort Collins, CO 80523-1371.

E-mail: nathan@atmos.colostate.edu

2006); and influence the timing of El Niño onset and decay (McPhaden 1999; Hendon et al. 2007). Anticipating future changes in the MJO is therefore of great interest to society.

The MJO may also help explain notable features of past climates. The MJO is known to excite Rossby waves that, in propagating to higher latitudes, transfer westerly momentum into the tropics and drive the atmosphere toward a superrotating state (Lee 1999; Grabowski 2004; Caballero and Huber 2010). This has been proposed as an explanation for the Pliocene “permanent El Niño,” an apparent disappearance of the equatorial cold tongue from 2 to 5 Ma (Wara et al. 2005; Fedorov et al. 2013; however, see Zhang et al. 2014). If MJO activity were enhanced in the (2–3 K) warmer Pliocene climate (Dowsett et al. 2011), this would lead to more tropical momentum convergence, weakening the equatorial easterlies and allowing the east–west Pacific thermocline slope to relax and thereby explaining the observed warm anomalies in the Pliocene east Pacific (Tziperman and Farrell 2009).

Our understanding of MJO dynamics remains incomplete, and any future change in MJO behavior is likely to depend on the future tropical mean state, itself an uncertain quantity. This combination makes projecting changes in MJO behavior a particularly challenging endeavor. Nevertheless, a number of studies have addressed this question with varying degrees of directness through examination of historical trends and numerical simulations.

Slingo et al. (1999) examined interannual variation in MJO activity in NCEP–NCAR reanalysis and the Hadley Centre Atmosphere Model, version 2a (HadAM2a) and found that, while year-to-year variability appears to be largely chaotic, decadal-scale changes suggest a dependence on temperature. MJO activity was consistently weaker prior to the mid-1970s, when sea surface temperatures (SSTs) were cooler. This led Slingo et al. to suggest that the MJO may become more active with global warming. These findings were echoed by Hendon et al. (1999) using a different methodology. Both studies found a weak relationship with ENSO, with relatively weaker MJO activity during warm phases and an eastward shift of intraseasonal variability past the date line. To the extent that a future pattern of warming is more or less “El Niño”-like (Yamaguchi and Noda 2006) or “La Niña”-like (Clement et al. 1996), this may also contribute to MJO changes.

More recently, Jones and Carvalho (2006) and Oliver and Thompson (2012) calculated MJO indices from reanalysis products over the last 50 and 100 yr, respectively, and both found weakly positive linear trends. Jones and Carvalho (2011) then developed a statistical

model of MJO activity trained to observations. When applied to late-twenty-first-century climate states from CMIP3 model projections, their model predicted significantly enhanced MJO activity.

Increased MJO activity in warmer climates has also been seen in numerical simulations. Lee (1999) found much stronger MJO activity after a prescribed increase in SST in an aquaplanet GCM. Caballero and Huber (2010) found that the NCAR Community Atmosphere Model, version 3 (CAM3) becomes dominated by an MJO-like mode at very high SST. Increases have also appeared in a high-resolution (40 km) version of ECHAM5 run with a CMIP3 A1B warming scenario (Liu et al. 2013), in the NCAR CCSM4 under the CMIP5 RCP8.5 high emissions scenario (Subramanian et al. 2014), and in the MPI ESM run with increased CO₂ (Schubert et al. 2013). On the other hand, an analysis of twenty-first-century simulations from 12 CMIP3 models found little agreement even on the sign of MJO change (Takahashi et al. 2011). However, this set of models is known to have low MJO simulation skill (Lin et al. 2006), so their lack of agreement is perhaps unsurprising. Maloney and Xie (2013) found that MJO activity in a modified version of CAM3 is sensitive to the spatial pattern of warming, which may also contribute to the intermodel spread in MJO changes.

There are theoretical reasons to suspect the MJO might intensify in warmer climates. One leading paradigm describes the MJO as a moisture mode, arising from feedbacks between convection and midtropospheric moisture (Raymond and Fuchs 2009; Sobel and Maloney 2012). Since atmospheric moisture content is expected to increase exponentially with temperature under the Clausius–Clapeyron relationship, one might suppose that at least the moist aspects of the MJO could scale at a similar rate. However, the relevance of moisture mode theory to the observed MJO remains an open question, and a specific mechanism causing MJO intensification with warming is not obvious.

Arnold et al. (2013) proposed a physical mechanism for MJO intensification based on a set of aquaplanet simulations with increasing SST. Analysis of the moist static energy budget linked the MJO increase to changes in vertical advection, which were due in turn to a steeper mean MSE profile at high SST. This steepening is linked to fundamental thermodynamics and is quite robust, but it can be offset by changes in the vertical velocity profile, which is less well constrained. It may be that the aquaplanet configuration is unrealistically favorable to MJO intensification.

Addressing this possibility, Arnold et al. (2014) recently reported a similar MJO intensification in simulations

with more realistic boundary conditions, including continents and a dynamic ocean. The present paper expands on their analysis and offers additional details. The model and experimental setup are described in [section 2](#). In [section 3](#), we compare the simulated mean state and MJO with observations. [Section 4](#) presents changes in the mean state and in MJO activity resulting from increased CO₂. In [section 5](#), we present a composite moist static energy budget and examine the physical processes sustaining the MJO and leading to intensification. Our conclusions are listed in [section 6](#).

2. Model description and experimental setup

The MJO has a reputation for being difficult to simulate, and most GCMs produce intraseasonal disturbances that are both too weak and too rapidly propagating ([Lin et al. 2006](#)). Our understanding of these deficiencies has improved over the last decade (e.g., [Thayer-Calder and Randall 2009](#)), with commensurate improvement in model MJO skill (e.g., [Neale et al. 2008](#)), though often at the expense of the tropical-mean climate ([Kim et al. 2011](#)). Here we use a superparameterized model, in which subgrid convective tendencies are explicitly generated by cloud system resolving models (CSRMs) embedded within each GCM column ([Grabowski 2001](#); [Randall et al. 2003](#)). Superparameterizations (or multiscale modeling frameworks; [Grabowski 2001](#)) have been implemented in several GCMs and show promising improvements to many aspects of convection (e.g., [Pritchard and Somerville 2009](#)). In the context of the historical challenge noted above, they are particularly noteworthy for their realistic portrayal of the MJO ([Grabowski 2004](#); [Benedict and Randall 2009](#); [Andersen and Kuang 2012](#); [Stan et al. 2010](#)), although its representation does appear to depend on the particular model version. This version dependence is poorly understood and may be related to differences in the tuning of unconstrained CSRMs parameters ([Pritchard and Bretherton 2014](#)), the use of different dynamical cores, or other unknown factors.

In this study, the host GCM is the NCAR Community Atmosphere Model, with the finite volume dynamical core and CAM4 physics on a $1.9^\circ \times 2.5^\circ$ horizontal grid with 30 levels in the vertical. This is run as the atmospheric component of the Community Earth System Model, version 1.0.2 (CESM1.0.2), coupled to dynamic ocean (POP2) and sea ice (CICE) models on a roughly $1.125^\circ \times 0.63^\circ$ grid, with a displaced pole. The embedded CSRMs are the System for Atmospheric Modeling, version 6 (SAM6; [Khairoutdinov and Randall 2003](#)), run with a two-dimensional domain consisting of 32 columns of 4-km width, oriented in the east–west direction, with

28 vertical levels collocated with the 28 lowest levels of CAM. The CSRMs use a single-moment five-species bulk microphysics scheme, as detailed by [Khairoutdinov and Randall \(2003\)](#).

To spin up the model, the conventional (non-SP) version of CESM was first run to steady state at pre-industrial (280 ppm) CO₂. The CO₂ concentration was then increased at 1% per year until quadrupling and then held steady for an additional 170 yr. Two superparameterized runs, denoted $1 \times \text{CO}_2$ and $4 \times \text{CO}_2$, were initialized from the end of the conventional simulations and run for an additional 16 and 13 yr, respectively. The final 10 yr in each case were used for all analysis presented in this paper.

At a given level of CO₂, the superparameterized CESM (SP-CESM) has a slightly cooler tropics than CESM; the tropical-mean temperatures in the last 10 yr of the SP-CESM $1 \times \text{CO}_2$ and $4 \times \text{CO}_2$ scenarios are 1.2 and 0.6 K cooler, respectively, than the corresponding equilibria in CESM. The last 10 yr show small linear cooling trends of less than 0.08 and 0.05 K yr⁻¹, relative to detrended interannual standard deviations of 0.2 and 0.15 K yr⁻¹. We therefore expect any remaining energy imbalance to have minimal effect on MJO behavior.

3. Mean state and MJO at $1 \times \text{CO}_2$

The annual-mean sea surface temperature from the preindustrial simulation is compared with the Reynolds SST climatology from 1971 to 2000 ([Reynolds et al. 2002](#)) in [Fig. 1](#). The model exhibits a widespread cold bias of roughly 1 K across the Indian Ocean and west Pacific and particularly around Central America. This is consistent with the finding of [Kim et al. \(2011\)](#) that models with a strong MJO signal, including the superparameterized CAM3.0, tend to have larger-than-observed surface fluxes when run with prescribed SST. In our simulations with a dynamic ocean, these excess air–sea fluxes may contribute to the cool SST bias. Isolated regions with a strong warm bias are also seen in the east Pacific, around the Humboldt and California Currents. The overall bias pattern is roughly constant across seasons, although the cold bias tends to be stronger in the subtropics in the summer hemisphere. A bias in the spatial pattern is potentially more problematic than one in the tropical mean, as it can distort the surface wind field and the patterns of mean precipitation and precipitation variance.

[Figure 2](#) shows the seasonal-mean precipitation and surface winds from observational datasets and the pre-industrial simulation. Here we use the GPCP precipitation climatology from 1979 to 2000 ([Adler et al. 2003](#)) and the NCEP–NCAR reanalysis from 1971 to 2000

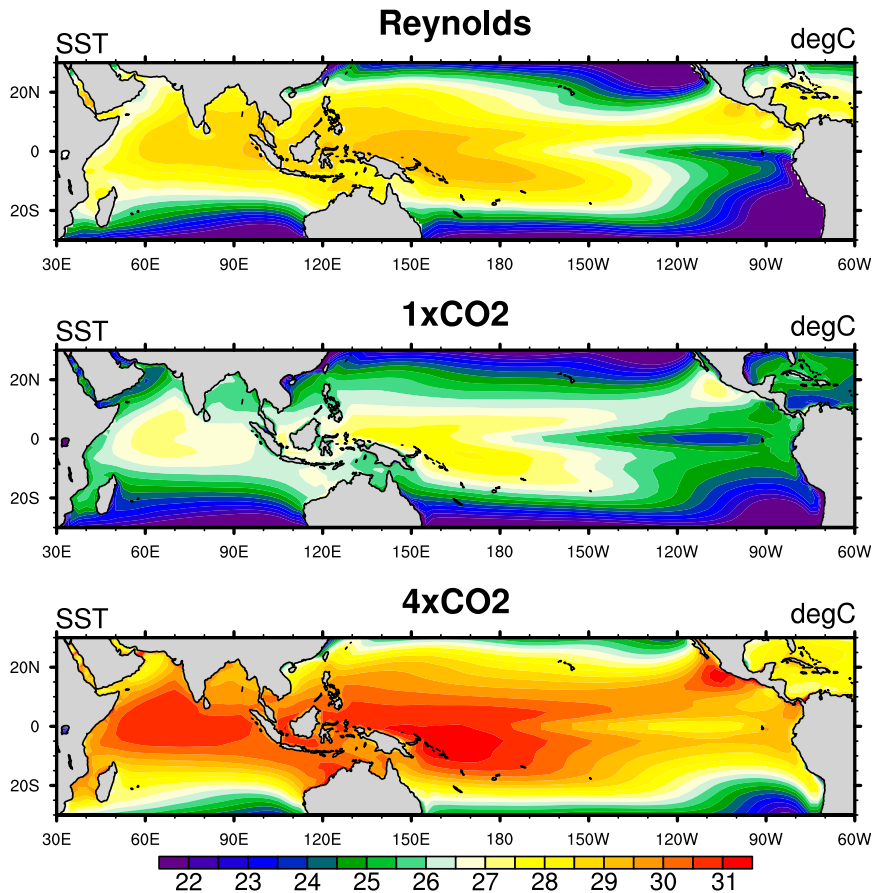


FIG. 1. Annual-mean SST from observations and $1\times\text{CO}_2$ and $4\times\text{CO}_2$ simulations. The $1\times\text{CO}_2$ fields qualitatively agree with observations, despite a pervasive 1-K cool bias. The $4\times\text{CO}_2$ case shows widespread warming.

(Kalnay et al. 1996). In the Pacific, the model has a pronounced double ITCZ that persists year-round, possibly associated with the east Pacific warm bias. Over the Indian Ocean, boreal winter precipitation is too intense and shifted too far west and an easterly bias is seen in the surface winds. In boreal summer, the model produces a reasonable Indian monsoon circulation and the Indian Ocean wind and precipitation biases are smaller. It is evident that adding superparameterized convection to a coupled atmosphere–ocean model does not immediately result in an improved mean state, as might have been hoped based on earlier successes (Stan et al. 2010).

Anomalous surface enthalpy fluxes induced by wind speed variation played a central role in early MJO theories (Emanuel 1987; Neelin et al. 1987); although these have been shown to be inconsistent with observations in their linear form, surface fluxes are still thought to be important to the MJO (Sobel et al. 2010). In nature, they are positively correlated with intraseasonal precipitation (Araligidad and Maloney 2008; Kiranmayi and

Maloney 2011), but their role in models is somewhat less consistent, playing a destabilizing role in some cases (Bellon and Sobel 2008; Grabowski 2003; Maloney and Sobel 2004) and weakening intraseasonal variance in others (Maloney 2002; Kim et al. 2011; Andersen and Kuang 2012). Areas of low-level westerlies over the Indian Ocean are thought to be important in maintaining the correct phasing between surface fluxes and precipitation in the MJO (Inness and Slingo 2003), and errors in the simulated mean state can therefore influence MJO instability and propagation (Zhang et al. 2006). In the SP-CESM $1\times\text{CO}_2$ case, the Indian Ocean surface winds are predominantly easterly and this may result in an unrealistic role for surface fluxes.

To assess the model MJO, we first compare the simulated tropical variability in outgoing longwave radiation (OLR) to the NOAA/NCEP Climate Prediction Center (CPC) product of interpolated satellite observations from 1981 to 2000 (Liebmann and Smith 1996). Equatorial wavenumber–frequency spectra shown in

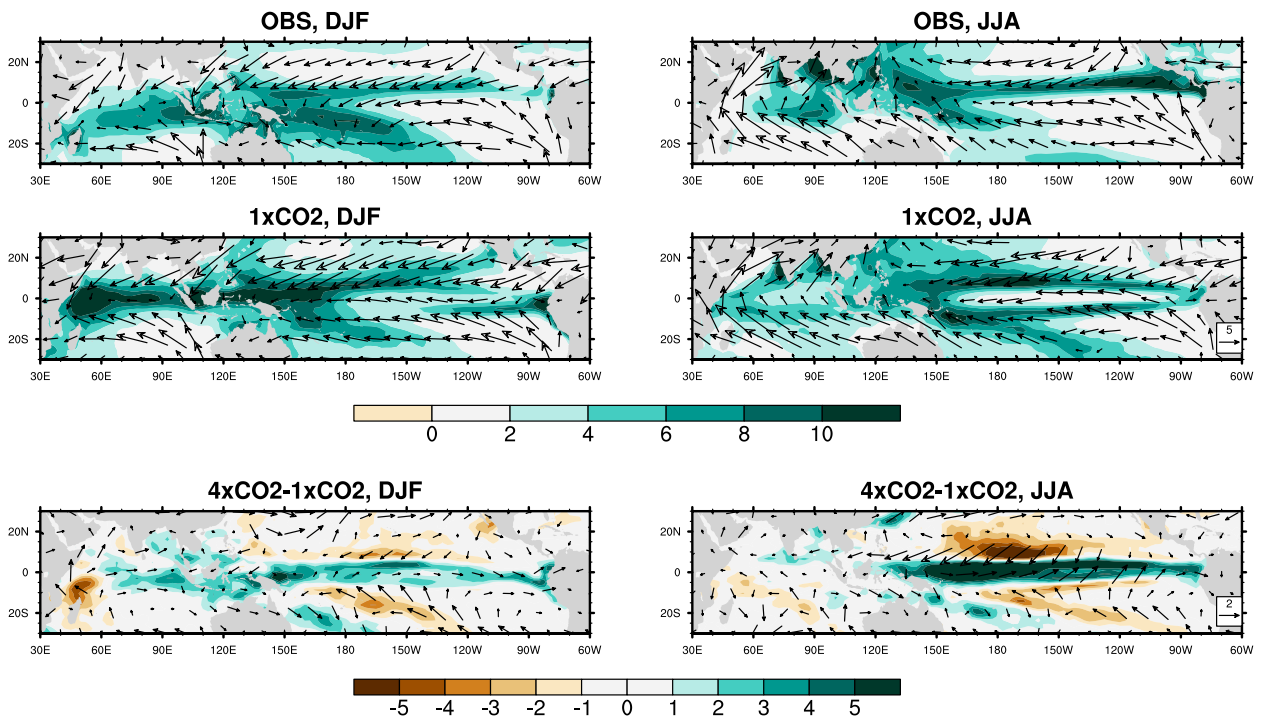


FIG. 2. (top),(middle) Seasonal-mean precipitation (mm day^{-1}) and surface winds from GPCP climatology, NCEP reanalysis, and the $1\times\text{CO}_2$ simulation. (bottom) The differences between $4\times\text{CO}_2$ and $1\times\text{CO}_2$. Reference wind vectors are shown in the bottom right of two panels.

Fig. 3 suggest that the model overestimates tropical variability at all scales relative to the CPC dataset, particularly for westward-moving disturbances. This westward bias has not been previously reported in superparameterized models, and its cause remains unknown, although unpublished work suggests it may be related to the finite volume dynamical core (C. DeMotte

2014, personal communication). The Kelvin, Rossby, and inertia-gravity wave bands show realistically elevated power relative to the inferred background spectrum, and simulated phase speeds agree with those observed, consistent with equivalent depths of 25–50 m (Wheeler and Kiladis 1999). Within the MJO band (defined in this paper as zonal wavenumbers 1–3 and

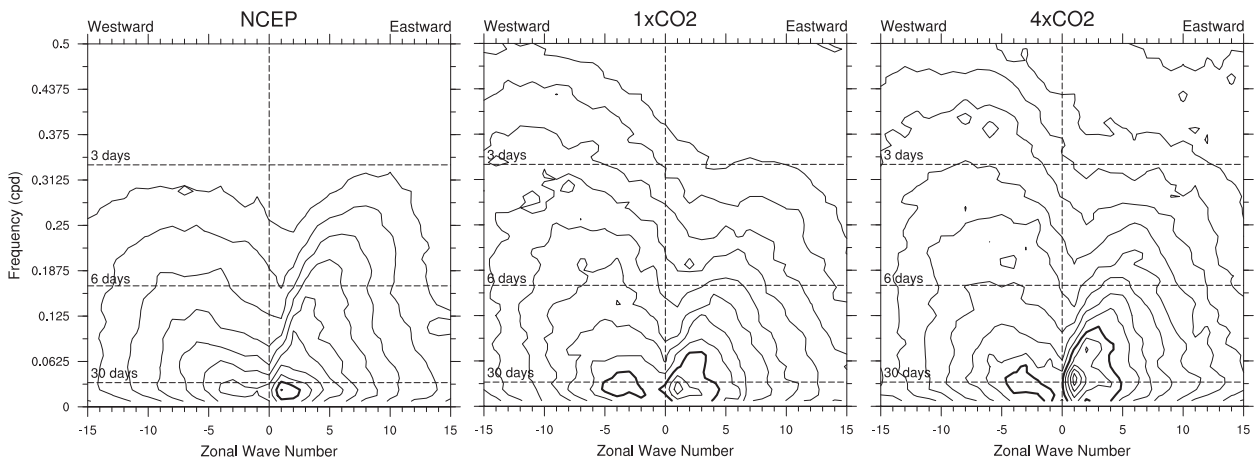


FIG. 3. Wavenumber–frequency equatorial power spectra of OLR from the NOAA-interpolated OLR dataset and $1\times\text{CO}_2$ and $4\times\text{CO}_2$ simulations. SP-CESM generally overestimates tropical OLR variability. A peak associated with the MJO is seen at $1\times\text{CO}_2$, which increases in magnitude and frequency at $4\times\text{CO}_2$. Contours show \log_{10} OLR power at intervals of $0.2 \text{ W}^2 \text{ m}^{-2}$, with the 1.2 contour in bold.

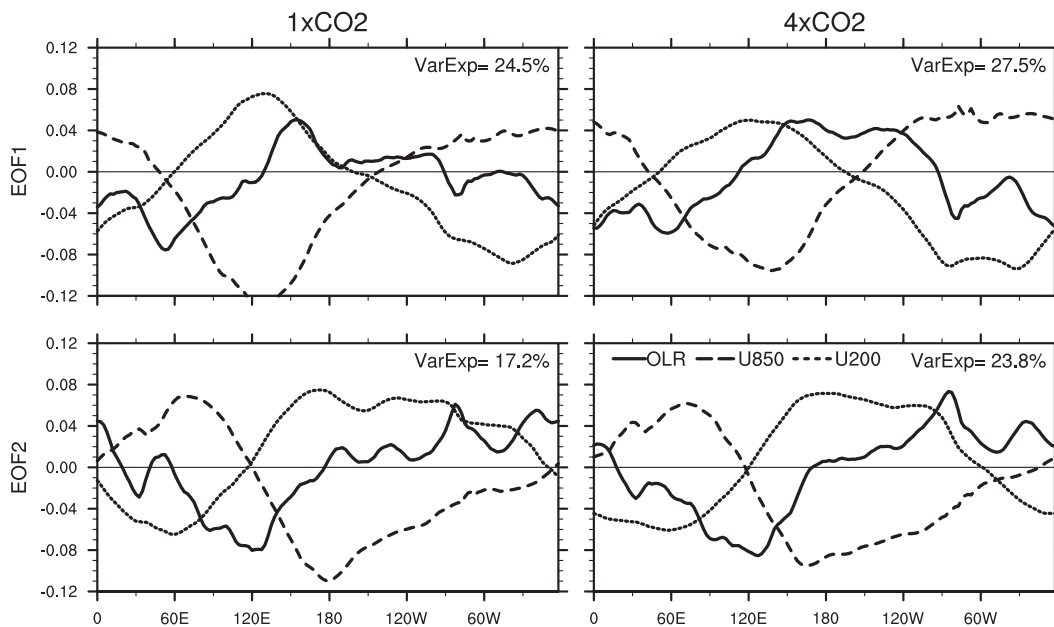


FIG. 4. The two leading combined EOFs of meridionally averaged OLR (solid), U850 (dashed), and U200 (dotted). The percentage of combined variance explained by each mode is indicated in the top right of each panel. The spatial structures are qualitatively similar in both cases, but the EOFs explain a larger fraction of the (larger) intraseasonal variance at $4\times\text{CO}_2$.

periods of 20–100 days), the OLR variance is stronger than observed, though the ratio of eastward to westward (negative wavenumbers) power is 1.9, compared with 2.7 in the CPC dataset. In contrast, the eastward/westward power ratio in precipitation is 2.8, compared with the GPCP-derived value of 2.0.

To evaluate the MJO's detailed spatial structure, we create composites of MJO anomalies using the method of Wheeler and Hendon (2004). Deviations from a daily climatology of 200-hPa zonal wind (U200), 850-hPa zonal wind (U850), and OLR are averaged in latitude between 15°S and 15°N , bandpass-filtered between 20 and 100 days, and then normalized by their respective zonal-mean temporal standard deviations. The two leading principal components (PCs) from a combined EOF analysis define an MJO index, with amplitude $\sqrt{\text{PC1}^2 + \text{PC2}^2}$ and phase angle determined from the PCs. In the $1\times\text{CO}_2$ run, the first two modes explain 41% of the combined-field intraseasonal variance and are maximally correlated ($r = 0.78$) at a lag of 9 days, indicating a 36-day period. The EOFs are shown in Fig. 4a. Their spatial structures resemble those derived from the NCEP–NCAR reanalysis (Wheeler and Hendon 2004) and change little in the $4\times\text{CO}_2$ case.

Composites are created by bandpass filtering anomalies and then averaging within each MJO phase during periods when the index amplitude exceeds 1. A composite of OLR, precipitation, and 850-hPa winds in

boreal winter (November–April) is shown in Fig. 5. The structure closely resembles composites of observations, with similar amplitude, primarily eastward propagation, and southward migration within the Pacific sector. Composites for boreal summer (May–October; not shown) show similar fidelity to observations. The pattern of intraseasonal variance is seen to migrate between hemispheres following the seasonal cycle, with peak variability in boreal winter and a secondary peak in boreal summer, in agreement with observations (Zhang and Dong 2004).

We conclude that, despite some differences between the modeled and observed mean states, SP-CESM simulates a robust MJO at $1\times\text{CO}_2$, with generally realistic variance, spatial structure, propagation, and seasonality.

4. Mean state changes and MJO intensification with warming

The tropical-mean surface temperature is 4.2 K warmer in the $4\times\text{CO}_2$ simulation, with enhanced warming in the east Pacific cold tongue along the coasts of South and Central America and in the subtropics of the summer hemisphere (Fig. 1). Precipitation over the Pacific increases primarily along the northern ITCZ, which appears to contract and shift toward the equator (Fig. 2). We note that this narrow band of increased precipitation is also seen in the CMIP5 multimodel mean, although

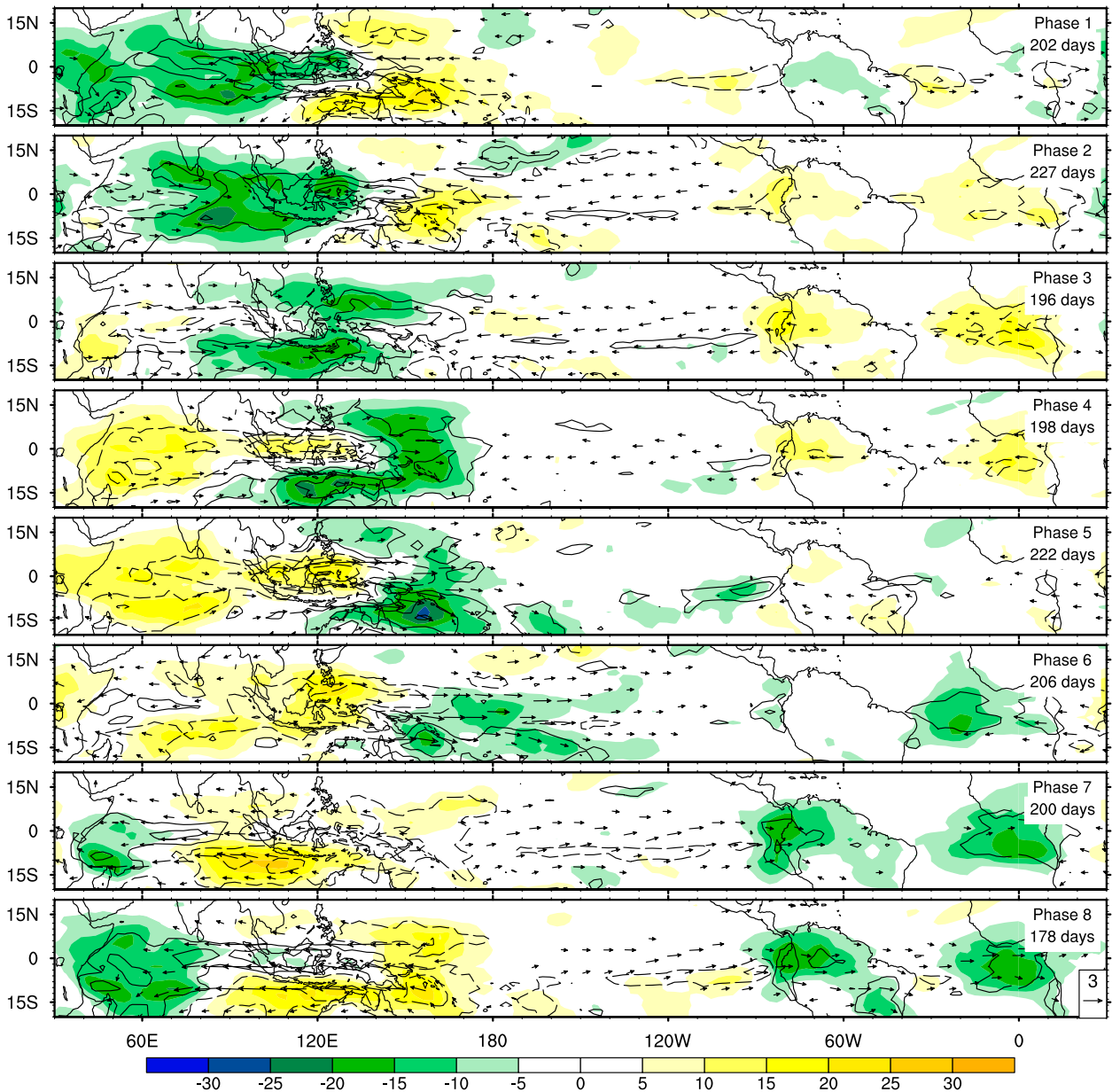


FIG. 5. Composite OLR (colors), precipitation (contours), and 850-hPa wind anomalies averaged within each MJO phase for the $1\times\text{CO}_2$ simulation. Precipitation contour interval is 2 mm day^{-1} . The MJO phase and number of days included in each average are indicated in the top right of each panel. A 3 m s^{-1} reference vector is shown in the bottom right, and vectors smaller than 1 m s^{-1} are not shown to improve clarity.

the off-equatorial pattern of drying is not (Stocker et al. 2014). Boreal winter precipitation over the western Indian Ocean is reduced, and the easterly surface winds are weakened. The winter hemisphere Hadley cells intensify while the summer hemisphere cells weaken, and the Walker circulation is stronger year-round (not shown).

The magnitude of MJO activity is typically estimated from the intraseasonal variance in fields associated with

moist convection (e.g., OLR, precipitation). Because these variables scale differently with warming, we list several metrics for each field in Table 1 in order to provide a more comprehensive summary. The total longitudinal-temporal standard deviation of each field, averaged between 10°S and 10°N , is listed to provide a measure of the background variability, while the standard deviation within the MJO band (zonal wavenumbers 1–3; periods of 20–100 days) and the ratio of

TABLE 1. Metrics of tropical variability based on daily precipitation (mm day^{-1}), OLR (W m^{-2}), and U850 (m s^{-1}). Shown are the total and MJO-band ($k = 1\text{--}3$; $P = 20\text{--}100$ days) longitudinal–temporal standard deviations and the ratio of eastward to westward MJO-band variance. Precipitation and OLR show increases in total variability, with larger fractional increases within the MJO band. Total zonal wind variability decreases, but a small increase is seen within the MJO band. The number of events per year identified from the Wheeler–Hendon index increases from 4.4 to 5.6.

	Precipitation			OLR			U850			Events per year
	Tot	MJO	E/W	Tot	MJO	E/W	Tot	MJO	E/W	
$1\times\text{CO}_2$	4.46	0.81	1.67	28.7	6.52	1.38	3.34	1.25	1.65	4.4
$4\times\text{CO}_2$	6.28	1.27	2.20	32.2	8.65	1.80	3.36	1.27	1.81	5.6

eastward to westward MJO-band variance (E/W) provide a measure of MJO-related variability. These numbers were calculated by averaging each field in latitude, calculating the wavenumber–frequency power spectrum, integrating over the desired wave band, and then taking the square root.

The standard deviation of total precipitation scales at roughly 7% per 1 K of warming, while within the MJO band the scaling is somewhat larger, at $9.5\% \text{ K}^{-1}$. We note that the global-mean precipitation, being subject to energetic constraints (Held and Soden 2006), scales at a more modest $2\% \text{ K}^{-1}$. The total OLR standard deviation also increases at roughly $3\% \text{ K}^{-1}$, with a larger increase of $8\% \text{ K}^{-1}$ in the MJO band. By contrast, the total zonal wind variability decreases, though the intraseasonal band still shows a small increase. This relative insensitivity of wind variability to warming was also noted by Maloney and Xie (2013), who attributed it to increases in static stability which make anomalous convective heating less efficient at inducing wind anomalies.

It is apparent that the convective aspects of the MJO intensify, but these are also embedded within a more variable background state. Interestingly, at $4\times\text{CO}_2$ the two leading EOFs explain 51% of the intraseasonal variance, compared with 42% at $1\times\text{CO}_2$. Thus, not only does intraseasonal variance increase, it also appears to be more structured. Using this coherent fraction of combined intraseasonal variance would suggest an even sharper rise in MJO activity.

The increases in MJO convective variance come in the form of both a greater number of events and a larger amplitude per event. The $4\times\text{CO}_2$ composite of anomalous OLR and precipitation is shown in Fig. 6, and comparison with Fig. 5 makes the increase in amplitude evident. To count individual MJO events, we use a metric based on the MJO index defined above. Events are defined for each active period in which the index amplitude remains above one and during which the MJO phase progresses eastward through at least 180° . For cases of multiple events in sequence, with the index amplitude remaining above one, we round the total phase progression to the nearest multiple of 360° . That

is, one event is indicated by $180^\circ < \Delta\phi < 539^\circ$, two events are indicated by $540^\circ < \Delta\phi < 899^\circ$, and so on.

The criteria above yield 4.4 events per year at $1\times\text{CO}_2$, and 5.6 events per year at $4\times\text{CO}_2$, with interannual standard deviations of 1.4 and 1.9 events per year, respectively. Although the absolute numbers change somewhat, depending on the choice of minimum amplitude and phase progression, the 20%–30% increase in event number between $1\times\text{CO}_2$ and $4\times\text{CO}_2$ is insensitive to parameter choice. The total number of days on which the Wheeler–Hendon index is above 1.0 decreases slightly from 2062 to 2042, while the average index amplitude during identified MJO events increases from 2.99 to 3.16. However, because the index is based on zonal wind and OLR that have been normalized by their respective standard deviations, this likely underestimates the actual change in magnitude of MJO-related anomalies. We also find that the mean length of a full 360° oscillation decreases from 42 to 33 days. This is likely associated with an increase in eastward propagation speed, clearly visible in lag-correlation plots (Fig. 7). These also indicate a much stronger intraseasonal precipitation signal over the central Pacific.

5. Moist static energy budget and intensification mechanism

Confidence in the real-world applicability of the simulated MJO increase might be enhanced by identifying physical connections between the changes in the MJO and changes in the mean state believed to be robust. To this end, we calculate the MSE budget of a composite MJO event. This analysis is based on the idea that the MJO is a moisture mode, depending fundamentally on variations in atmospheric water vapor (Bladé and Hartmann 1993; Fuchs and Raymond 2002; Sobel and Maloney 2012); unlike the spectrum of equatorial shallow water waves (Matsuno 1966), a moisture mode has no equivalent in a dry atmosphere.

An important factor in moisture mode instability is the sensitivity of deep convection and precipitation to environmental humidity. In a dry environment, turbulent

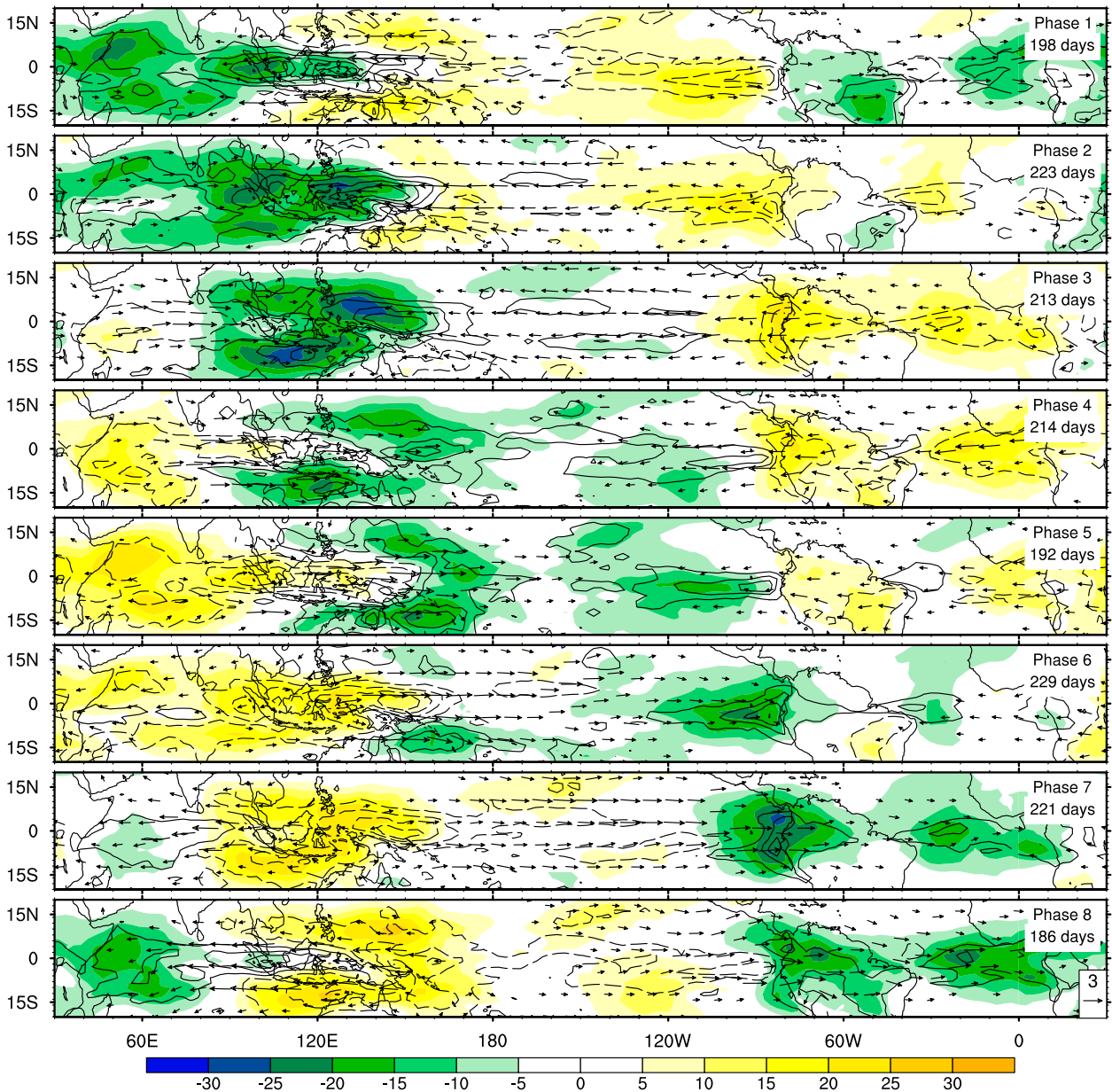


FIG. 6. As in Fig. 5, but for $4\times\text{CO}_2$. The OLR and precipitation anomalies in most phases are visibly larger than in the $1\times\text{CO}_2$ case, particularly over the Pacific.

entrainment of dry environmental air will rapidly deplete the buoyancy of a convecting plume and inhibit precipitation (Derbyshire et al. 2004). By contrast, an anomalously moist environment will allow strong precipitation and convective heating. This dynamic likely explains the strong relationship between precipitation and column moisture seen in nature (Bretherton et al. 2004). Under the weak temperature gradient (WTG) conditions prevailing in the tropics (e.g., Sobel et al. 2001), any anomalous heating is rapidly balanced by adiabatic ascent and cooling. Advection by the induced

circulation will affect the column MSE, with a net effect depending on the gross moist stability (GMS; Neelin et al. 1987; Raymond and Fuchs 2009), a measure of the efficiency of column MSE export. The GMS is the residual of moist static energy export at upper levels and import at low levels. An effective GMS, including radiative and surface flux feedbacks, can also be defined. A moisture mode instability can occur if this effective GMS is negative, that is, if anomalous convection leads to a net increase in column MSE. A moisture anomaly would then be amplified by the combined feedbacks,

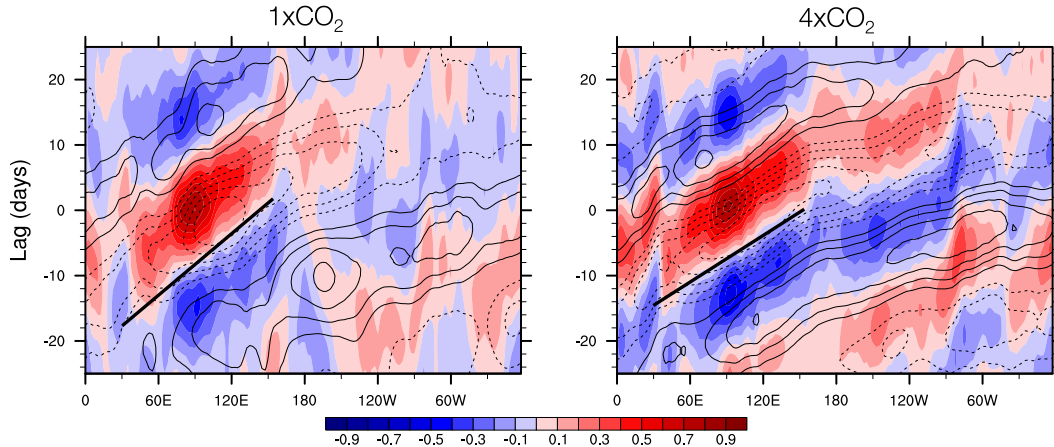


FIG. 7. Correlation of intraseasonal 10°S–10°N precipitation (colors) and U850 (contours) with precipitation averaged over a base region (5°S–10°N, 80°–100°E) for various lags. At 4×CO₂ the intraseasonal anomalies show greater coherency and faster eastward propagation. Black solid lines indicate speeds of 8.3 and 11 m s^{−1}. The precipitation contour interval is 0.1, and negative contours are dashed.

setting up a self-sustaining anomaly of convection and circulation. In this paradigm, eastward propagation of the MJO results from a zonal asymmetry in the sources and sinks of MSE.

These ideas have led many authors to examine composite MSE budgets generated from reanalysis products (Kiranmayi and Maloney 2011) and model output (Maloney 2009; Andersen and Kuang 2012; Arnold et al. 2013). Such studies have provided a general account of the flow of MSE within the MJO, although with some disagreement because of differences in methodology and data. Points of agreement include eastward propagation driven by a combination of horizontal and vertical advection, with greater weight given to the vertical component in reanalysis products (Kiranmayi and Maloney 2011). The horizontal component is associated both with slow Rossby gyres to the west of the MSE maximum and with suppression (enhancement) of synoptic eddies east (west) of the MSE maximum, which otherwise constitute an MSE sink by mixing air with the relatively dry subtropics (Maloney 2009; Andersen and Kuang 2012). In models and observations, MSE anomalies tend to covary with longwave radiative heating anomalies due to OLR suppression by high clouds.

In this study, we use the frozen MSE, which is defined as

$$h = c_p T + gz + L_v q - L_i q_i,$$

where c_p is the specific heat at constant pressure, T is temperature, g is gravity, z is geopotential height, L_v is the latent heat of vaporization, q is the water vapor mixing ratio, L_i is the latent heat of freezing, and q_i is the ice mixing ratio. This quantity is nearly conserved for air

parcels undergoing phase changes between vapor, liquid, and ice; the effect of small-scale convection is simply to redistribute MSE within a column. We use the pressure-weighted vertical integral of MSE,

$$\langle h \rangle = \frac{1}{g} \int_{p(\text{bot})}^{p(\text{top})} h dp,$$

for which the net effect of convection is nearly zero. The vertically integrated MSE tendency,

$$\begin{aligned} \langle \partial_t h \rangle = & -\langle \mathbf{u} \cdot \nabla h \rangle - \langle \omega \cdot \partial_p h \rangle + \langle \text{LW} \rangle + \langle \text{SW} \rangle \\ & + \text{LHF} + \text{SHF}, \end{aligned}$$

is controlled by horizontal and vertical advection, longwave (LW) and shortwave (SW) radiative heating, latent surface heat fluxes (LHF), and sensible surface heat fluxes (SHF). Similar to previous studies (Andersen and Kuang 2012; Arnold et al. 2013; Benedict et al. 2014), we diagnose the advective terms offline, using 6-h averages. Because of differences in numerics and to the neglect of rapid (<6 h) eddy transport, this necessarily introduces some error relative to the model's internally calculated advection. However, these errors appear to be small, and we show in the next section that the composite MSE budget is nearly closed.

To give a sense of their spatial structure, Fig. 8 presents each composite budget term averaged over phase 2 of MJO events during boreal winter (November–April), when the MSE maximum is around 110°E. A positive MSE tendency is seen over a broad region to the east and southward, with a negative tendency to the west. The MSE anomaly is noticeably in phase with the longwave heating

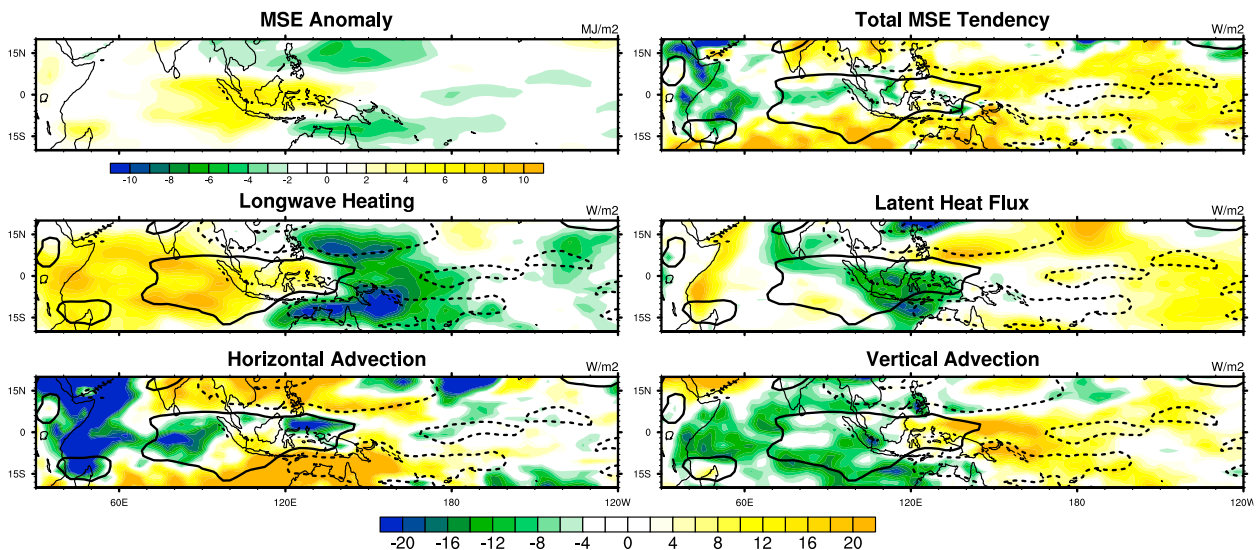


FIG. 8. Composite MSE budget terms averaged over MJO phase 2 for boreal winter at $1\times\text{CO}_2$. A positive MSE anomaly is centered over Indonesia. Contours of $\pm 2 \text{ MJ m}^{-2}$ MSE are overlaid on the tendency plots to aid interpretation. The negative contour is dashed. The phasing between MSE and tendency terms suggests the importance of longwave anomalies for maintaining the MJO and of advection anomalies for eastward and poleward propagation.

pattern and out of phase with the advection and surface flux terms. Since the anomalous longwave heating appears to add to regions with anomalously high MSE, and remove MSE from low anomalies, it therefore serves as an energy source. Similarly, advection and surface fluxes tend to decrease the MSE anomaly pattern, indicating an energy sink. The pattern of vertical advection, similar to the MSE anomaly but shifted roughly one quarter cycle to the east, suggests a strong contribution to eastward propagation, while the horizontal tendencies suggest propagation toward the poles. This differs somewhat from previous modeling studies, which found a significant contribution from horizontal advection to eastward propagation (Maloney 2009; Andersen and Kuang 2012; Arnold et al. 2013).

The evolution of each term in time is illustrated in Fig. 9. Each term is meridionally averaged between 10°S and 10°N and shown as a function of MJO phase and longitude. Eastward propagation is clearly visible, as positive MSE anomalies develop over the Indian Ocean in phase 6, intensify over the Maritime Continent in phase 2, and dissipate over the Pacific in phase 5. As in Fig. 8, longwave anomalies appear largely in phase with MSE and advective terms are out of phase. Surface fluxes appear to be weaker than in Fig. 8, but this is an artifact of meridional averaging, which leads to a partial cancellation of positive and negative anomalies. This illustrates a limitation of the two-dimensional graphical analysis (cf. Maloney et al. 2010; Kim et al. 2014), which is avoided in the quantitative method described below.

To better estimate the importance of each budget term to amplifying or damping the MJO anomalies, we use an adapted form of the method of Andersen and Kuang (2012). Anomalies from daily climatologies are bandpass filtered to retain intraseasonal (20–100 days) periods and zonal wavenumbers 1–6. The fractional growth rate of the anomalous pattern of MSE ($\langle h \rangle$) provided by a budget term ($\langle \Phi \rangle$) is given by the projection

$$F_\Phi = \frac{\iint \langle h \rangle \langle \Phi \rangle dA}{\iint \langle h \rangle^2 dA}, \quad (1)$$

where the area-weighted integral is taken over 15°S – 15°N and 60°E – 180° . This forcing F_Φ is calculated at every 6-h interval, and a composite is created by averaging over each MJO phase during active periods (index amplitude greater than one).

The result may be thought of as a budget of intraseasonal MSE variance, where the normalized variance tendency is equal to the sum of the forcings,

$$\frac{1}{2} \frac{\iint \partial_t \langle h \rangle^2 dA}{\iint \langle h \rangle^2 dA} = F_{\text{XAdv}} + F_{\text{YAdv}} + F_{\text{ZAdv}} + F_{\text{LW}} \\ + F_{\text{SW}} + F_{\text{LHF}} + F_{\text{SHF}}.$$

The budget thus quantifies the relative importance of each term, as well as changes in their importance between

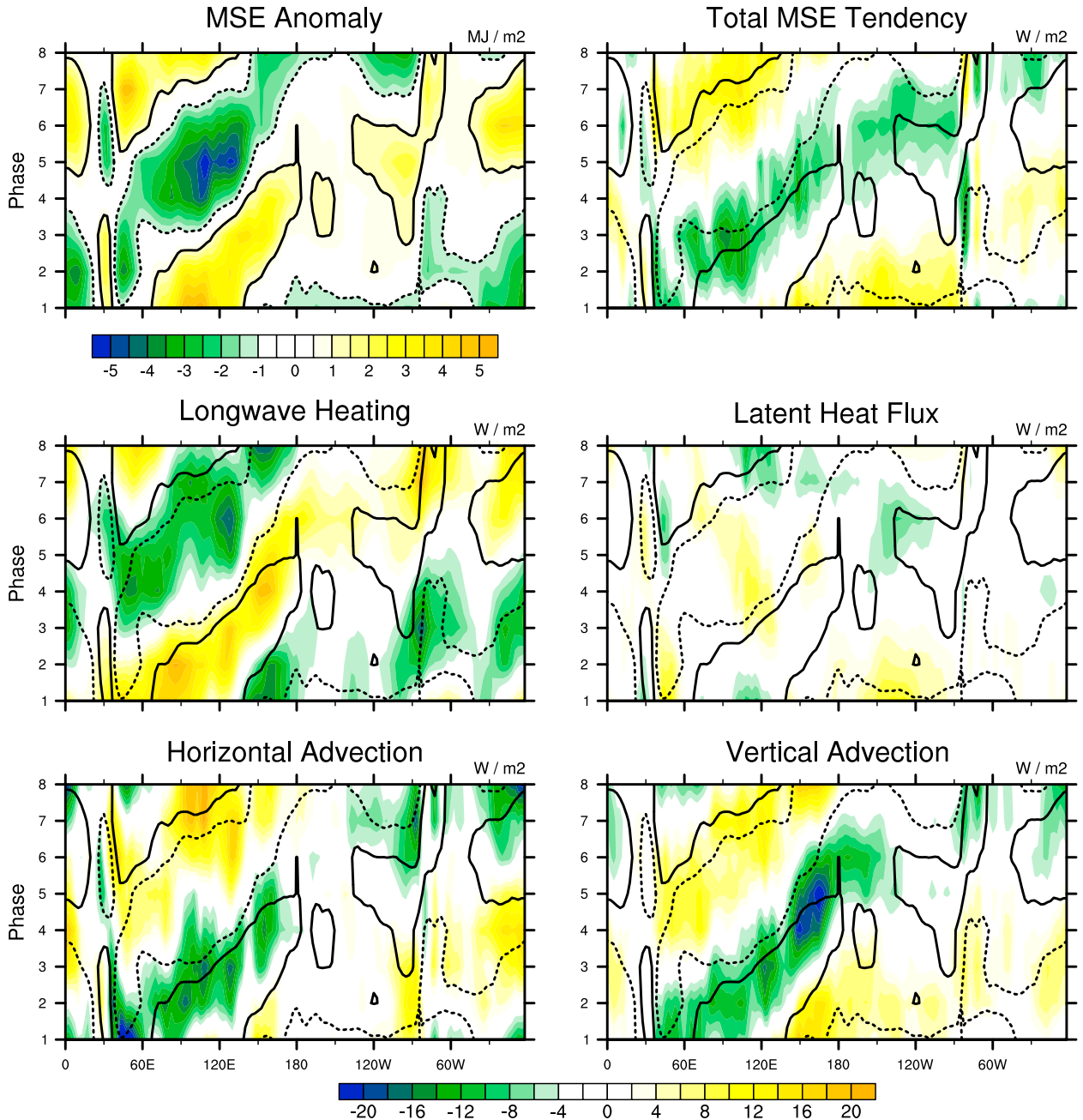


FIG. 9. Composite MSE budget terms averaged over 10°S – 10°N for boreal winter, plotted as a function of longitude and MJO phase. Contours of $\pm 1 \text{ MJ m}^{-2}$ MSE are overlaid on the tendency plots to aid interpretation. The negative contour is dashed.

$1\times\text{CO}_2$ and $4\times\text{CO}_2$. If their sizes, normalized by the MSE anomaly, remain constant, this would indicate no change in the balance of processes maintaining the MJO. Given the increase in MJO activity documented in section 3, we will focus our attention on terms that become more positive (more destabilizing) with warming.

The $1\times\text{CO}_2$ MSE variance budget (Fig. 10) is similar to those in previous studies. The MJO in SP-CESM is

principally supported by suppressed longwave cooling associated with high clouds around the MSE maximum and damped by suppressed surface latent heat fluxes associated with enhanced surface humidity. Zonal advection acts as a source of MSE variance, while meridional advection is a strong sink.

At high CO_2 , the MJO remains principally supported by longwave anomalies and damped by surface latent

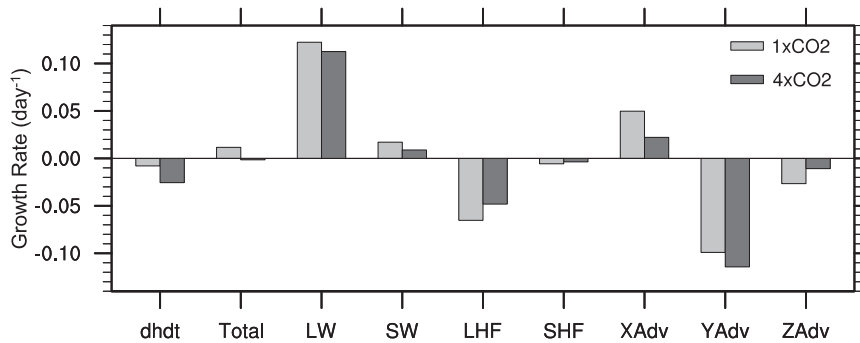


FIG. 10. Estimates of the contribution F_{Φ} of each budget term Φ to maintenance/dissipation of the MSE anomaly, for $1\times\text{CO}_2$ (light) and $4\times\text{CO}_2$ (dark). Visible are the dominant roles of longwave radiation (LW) and meridional advection (YAdv) in maintaining and dissipating the MJO, respectively. Surface fluxes and vertical advection (ZAdv) become more positive with warming, likely contributing to the stronger MJO. These positive shifts are ultimately balanced by zonal (XAdv) and meridional advection.

heat fluxes, but the effective growth/decay rates they provide per unit MSE have decreased in magnitude. Of special interest in this study are the significant positive shifts seen in latent heat flux and vertical advection. If either change resulted from the warmer tropical mean state, it could potentially explain the stronger simulated MJO. However, making such a claim requires us to identify a physical mechanism linking changes in the budget to the altered mean state. In pursuit of such a mechanism, we now examine each of these terms in greater detail.

a. Vertical advection decomposition

To gain insight into the vertical advection term, we decompose the vertical velocity and vertical MSE gradient into climatology, intraseasonal (20–100 days) and residual components as in Arnold et al. (2013), such that

$$\omega = \bar{\omega} + \omega^{\text{IS}} + \omega^r, \quad \frac{\partial h}{\partial p} = \frac{\partial \bar{h}}{\partial p} + \frac{\partial h^{\text{IS}}}{\partial p} + \frac{\partial h^r}{\partial p}.$$

The product of ω and $\partial h/\partial p$ yields nine terms. Taking the projection of each term onto the MSE anomaly for both model runs, we find that the change in vertical advection is entirely associated with the intraseasonal velocity acting on the climatological MSE. This term was also identified in the aquaplanet simulations of Arnold et al. (2013), who attributed the change to a deepening of the midtropospheric MSE minimum relative to the surface in warmer climates. This is a simple consequence of maintaining a moist adiabat over a warmer surface with minimal change in the relative humidity profile. This leads to an increase in $\partial h/\partial p$ in the lower troposphere, which promotes MSE accumulation in regions of anomalous ascent (where $\omega < 0$) and decreases MSE in regions

of descent. Since regions of ascent within the MJO are associated with high MSE and regions of descent are associated with low MSE, the change in vertical advection provides a positive feedback on MJO growth.

This mechanism also appears to be at work in the current simulations. Vertical profiles of MSE averaged over the Indian Ocean and west Pacific between 10°S and 10°N are shown in Fig. 11 and indicate a similar deepening of the midtropospheric minimum. We argue that this steepening effect again plays an important role in the simulated MJO intensification. Further, it offers an explanation for the faster eastward propagation and shortened MJO period at $4\times\text{CO}_2$. Projections of budget terms on the column MSE tendency $\partial h/\partial t$, given by

$$T_{\Phi} = \frac{\iint \langle \partial_t h \rangle \langle \Phi \rangle dA}{\iint \langle \partial_t h \rangle^2 dA},$$

are shown in Fig. 12. In this case, by far the largest change is a positive shift in vertical advection. This can be understood by referring to the vertical velocity profiles in Fig. 13, averaged over 5°S – 5°N during MJO phase 2 of boreal winter. The regions of positive MSE tendency east of the MSE maximum (as seen in Fig. 8) coincide with regions of shallow large-scale ascent and weak upper-level descent. This shallow ascent would be vertically advecting only the positive $\partial h/\partial p$ of the lower troposphere, while the upper-level descent would act on the negative $\partial h/\partial p$ of the upper troposphere, with both contributing to an increase in the column MSE. The enhanced vertical MSE gradients at $4\times\text{CO}_2$ would therefore increase the contribution of vertical advection to the eastward MSE tendency.

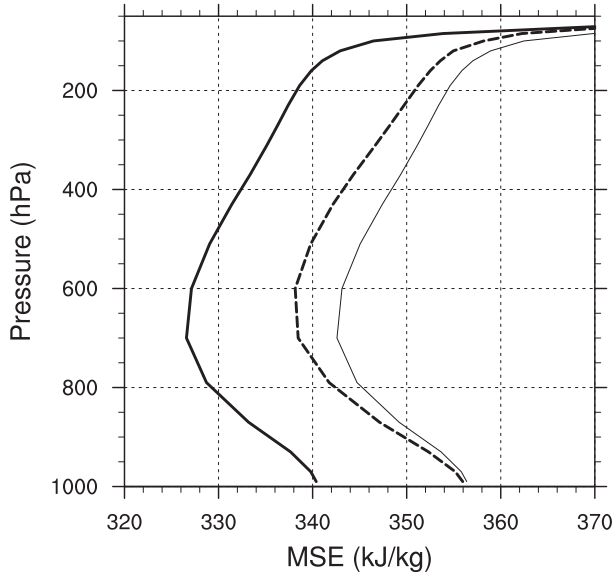


FIG. 11. Vertical profiles of MSE averaged over time, 10°S – 10°N and 60°E – 180°E , for the $1\times\text{CO}_2$ (solid) and $4\times\text{CO}_2$ (dashed) simulations. The $1\times\text{CO}_2$ profile is also shown shifted by 15.6 kJ (thin) to match the $4\times\text{CO}_2$ profile at the surface and emphasize the difference in vertical gradients.

b. Surface latent heat flux decomposition

Figure 10 suggests that an increase in surface latent heat flux also contributes to the stronger MJO activity, but it is unclear if this represents a primary cause of the MSE strengthening or a positive feedback. To better understand the surface flux scaling, we perform a decomposition based on the bulk formula

$$\text{LHF} = C_E \rho |v| (q_s - q) = C_E \rho |v| q_s (1 - \text{RH}).$$

Although in the model C_E is a function of the low-level stability, in our calculations we use a fixed value of $1690\text{ m}^2\text{ s}^{-1}$, determined by the method of least squares to minimize the differences between our estimated fluxes and those diagnosed within the model. The bulk formula applies only over ocean; fluxes over land are determined within the land model (CLM4). We therefore limit this decomposition to ocean-only grid boxes. Forcing estimates for each term are calculated as before, but with land boxes excluded from the area integral. The sum of these estimates differs slightly from the total surface flux forcing shown in Fig. 10, but we believe this decomposition captures the primary factors behind the change in forcing.

We define an absolute surface moisture deficit, $q_d = q_s(1 - \text{RH})$, and then decompose the wind speed and moisture contributions, again according to

$$q_d = \bar{q}_d + q_d^{\text{IS}} + q_d^r, \quad |v| = |\bar{v}| + |v|^{\text{IS}} + |v|^r.$$

As in the vertical advection decomposition above, this yields nine terms. In this case, most of these are negligible, and the only two significant terms are shown in Fig. 14. This shows that, in both the $1\times\text{CO}_2$ and $4\times\text{CO}_2$ scenarios, the latent heat flux contribution to intraseasonal MSE variations is almost entirely due to the term $C_E \rho |\bar{v}| q_d^{\text{IS}}$, representing the latent heat flux due to a combination of climatological surface winds and intraseasonal variation of the surface moisture deficit. A secondary decomposition of the moisture deficit term using

$$q_s = \bar{q}_s + q_s^{\text{IS}} + q_s^r \quad 1 - \text{RH} = (1 - \overline{\text{RH}}) - \text{RH}^{\text{IS}} - \text{RH}^r$$

further indicates that, again at both CO_2 levels, the contribution from surface moisture variations is entirely associated with relative humidity, rather than changes in the saturation specific humidity. This suggests that regions of anomalously high MSE and correspondingly high relative humidity result in suppressed surface evaporation which tends to damp the MSE anomaly.

This is in contrast with the classical WISHE mechanism for MJO growth, which relies on variations in wind speed to regulate surface evaporation (Emanuel 1987; Neelin et al. 1987). Instead, although we find that the intraseasonal variations in wind speed and relative humidity deficit are both roughly 10% of their mean values, the spatial pattern of wind speed anomalies is very weakly correlated with the MJO MSE anomalies at both $1\times\text{CO}_2$ and $4\times\text{CO}_2$ and thus has little net contribution to intraseasonal MSE growth or decay.

Now considering the change in F_{LHF} between $1\times\text{CO}_2$ and $4\times\text{CO}_2$, we find that it is again entirely captured in the two leading terms shown in Fig. 13: $C_E \rho |v|^{\text{IS}} \bar{q}_d$ and $C_E \rho |\bar{v}| q_d^{\text{IS}}$. That is, the intraseasonal wind speed anomaly and climatological moisture deficit and the climatological wind speed and intraseasonal moisture deficit. In the $4\times\text{CO}_2$ case, $C_E \rho |v|^{\text{IS}} \bar{q}_d$ becomes slightly more negative and thus slightly weakens the MJO. In contrast, $C_E \rho |\bar{v}| q_d^{\text{IS}}$ becomes significantly more positive and appears to explain the overall reduction in damping from surface fluxes. The secondary decomposition using q_s and RH again indicates that q_d^{IS} is mostly associated with relative humidity variation.

The forcing estimates calculated from Eq. (1) can be approximated by the spatial correlation between MSE and each term, scaled by the ratio of their spatial standard deviations,

$$F_{\Phi} \approx r_{h,\Phi} \left(\frac{\sigma_{\Phi}}{\sigma_h} \right).$$

Using this approach, we find that the forcing from $C_E \rho |v|^{\text{IS}} \bar{q}_d$ becomes more negative at $4\times\text{CO}_2$ largely

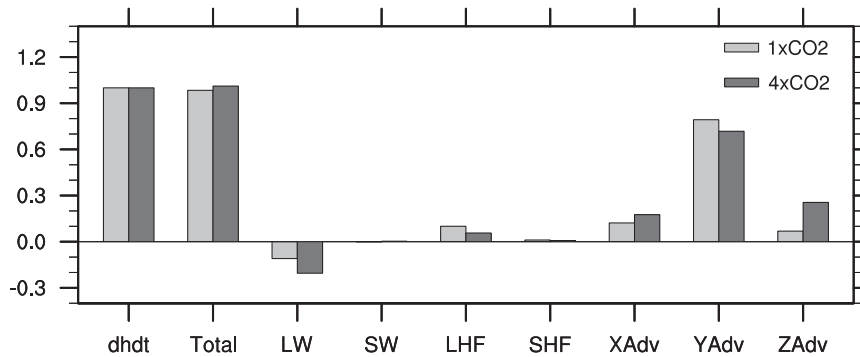


FIG. 12. Fraction of the total MSE tendency provided by each budget term for $1\times\text{CO}_2$ (light) and $4\times\text{CO}_2$ (dark). The tendency in both cases is dominated by YAdv, but ZAdv contributes a larger share of the total at $4\times\text{CO}_2$.

because the correlation decreases from $r = -0.03$ to $r = -0.08$.

The second component, $C_E \rho |\bar{v}| q_d^{\text{IS}}$, appears to change for two reasons: First, the correlation increases from $r = -0.44$ to $r = -0.33$, accounting for roughly two-thirds of the change in forcing. This may be connected to the westerly shift in mean Indian Ocean surface winds seen in Fig. 2. The remainder is due to a change in the relative magnitudes of q_d^{IS} and the MSE anomalies, which may be understood by a thermodynamic argument. Assuming similar relative humidity anomalies in both cases, the fluxes associated with q_d^{IS} should scale with the surface saturation specific humidity at $7\% \text{K}^{-1}$ or approximately 30% between $1\times\text{CO}_2$ and $4\times\text{CO}_2$. Meanwhile the standard deviation of the column MSE anomalies is found to increase by 40%; this implies that the surface fluxes simply cannot “keep up” with the increasing MSE anomalies, and their normalized forcing is reduced.

In summary, we find that the mechanism of MJO intensification likely works through the vertical advection term, whose forcing becomes increasingly positive with warming. This is due in part to a steepening of the mean MSE profile, which makes large-scale ascent more

effective at increasing the column MSE. This is particularly true in the region of shallow ascent to the east of the MSE maximum, offering a plausible explanation for the MJO’s faster eastward propagation at $4\times\text{CO}_2$. The change in forcing from surface latent heat flux is more ambiguous. Part of the change in forcing is due to an increase in correlation between fluxes and MSE anomalies, which may be linked to changes in the mean state and thus could be considered a primary cause of MJO intensification. The remainder appears to result from the surface flux anomalies being constrained to increase more slowly with SST than the column MSE anomalies and could therefore be seen as amplifying rather than causing the stronger MJO.

6. Conclusions

We examined the tropical intraseasonal variability in a pair of simulations with a superparameterized version of the Community Earth System Model, version 1.0.2 (CESM1.0.2) forced with preindustrial ($1\times$) and quadrupled ($4\times$) CO_2 . The $1\times\text{CO}_2$ simulation produces a leading mode of intraseasonal variability which closely

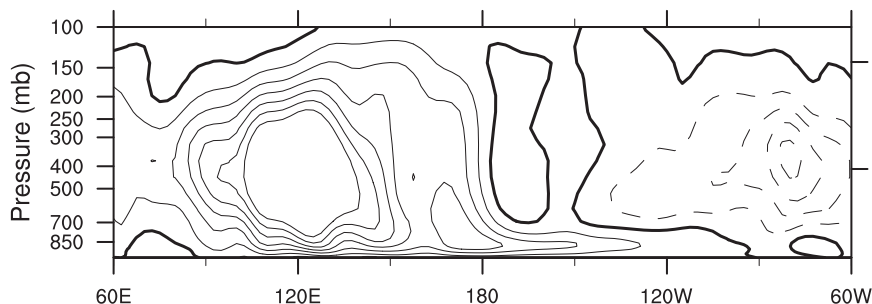


FIG. 13. Vertical pressure velocity anomalies (Pa s^{-1}) averaged over 5°S – 5°N in MJO phase 2 during boreal winter. A shallow ascent is seen to the east of the MSE maximum. The zero contour is bold, and positive contours (downward motion) are dashed.

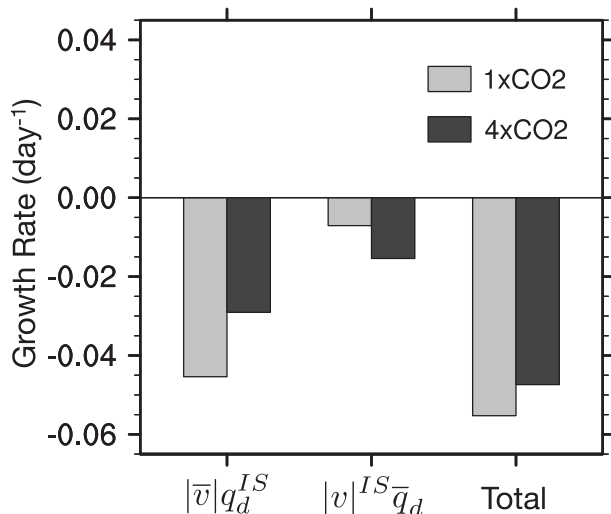


FIG. 14. The two leading terms contributing to surface latent heat flux forcing and the sum of all terms. This indicates the positive shift in total forcing is primarily due to $C_{EP}|\bar{v}|q_d^{IS}$.

resembles the observed Madden–Julian oscillation (MJO). The high CO₂ simulation results in a tropical-mean warming of 4.2 K and a significant increase in the variability of moist convection on all scales.

Variance within the MJO band increases faster than the background: for example, the standard deviation of MJO-band precipitation increases 10% per 1 K of tropical surface warming. A simple counting method based on the Wheeler and Hendon (2004) MJO index shows this increase manifests itself through a 20%–30% increase in the number of MJO events, as well as a greater magnitude of the anomalies in each event. More rapid eastward propagation is also seen.

Analysis of a composite budget of column moist static energy (MSE) indicates, similar to previous studies (Lin et al. 2004; Grodsky et al. 2009; Maloney 2009; Kiranmayi and Maloney 2011; Andersen and Kuang 2012), that the model MJO’s principal source of MSE is the longwave radiative anomaly associated with variation in high cloud fraction. This is balanced by an energy sink from surface latent heat flux anomalies, as high surface relative humidity suppresses evaporation in regions of high MSE. Likely because of biases in the modeled mean state, wind speed–induced surface flux anomalies are weakly correlated with MSE anomalies and have little contribution to MSE maintenance. Eastward propagation is primarily driven by a combination of horizontal and vertical advection and opposed by the radiative anomalies.

Changes between 1×CO₂ and 4×CO₂ in the MSE budget are interpreted here as changes in the MJO dynamics. We focus on vertical advection and surface

latent heat fluxes, the two terms whose normalized MSE forcing becomes increasingly positive with warming, suggesting that they play some role in enhancing the MJO activity. Inferring causality from a budget analysis is a difficult enterprise, but by linking changes in budget terms to robust (thermodynamic) changes in the mean climate state we have found further evidence for the MJO intensification mechanism first proposed by Arnold et al. (2013). As in that study, a decomposition of the vertical advection term indicates that the difference between 1×CO₂ and 4×CO₂ is associated with the intraseasonal vertical velocity acting on the climatological-mean MSE profile. This difference is attributed to a steepening of the MSE profile with warming, which results from maintaining a moist adiabat with minimal change in relative humidity. Although this steepening is a robust consequence of warming and is likely the primary cause of enhanced MJO activity in the 4×CO₂ simulation, its effect on vertical MSE advection can be offset by changes in the intraseasonal vertical velocity, which is itself poorly constrained. In other models or in nature, a sufficiently large upward shift in the velocity profile could limit or even reverse the change in vertical advection; this possibility limits the generality of the proposed intensification mechanism.

The decrease in damping from surface latent heat flux is shown to result from two effects. First, the fluxes become more weakly correlated with MSE anomalies, which may be linked with changes in the mean surface wind field. Second, the surface flux anomalies increase with warming approximately at the rate of the saturation specific humidity (7% K⁻¹), while the column MSE anomalies increase more rapidly, resulting in a proportionately weaker damping effect. We note that the MJO surface fluxes are affected by model biases in the mean surface wind field, and therefore the applicability of this analysis to the real world may be limited.

This work adds to existing evidence that MJO activity may increase in response to global warming. Evidence for an MJO dependence on SST has been identified in observations (Hendon et al. 1999; Slingo et al. 1999; Jones and Carvalho 2006; Oliver and Thompson 2012), and in some numerical models (Lee 1999; Caballero and Huber 2010; Arnold et al. 2013; Schubert et al. 2013). However, other models have shown negative or neutral trends with SST (Takahashi et al. 2011) or a strong dependence on the spatial pattern of warming (Maloney and Xie 2013), so any conclusions regarding future trends should be viewed as tentative.

If MJO activity were to intensify, it could affect many other climate phenomena, including ENSO (McPhaden

1999), tropical cyclogenesis (Hall et al. 2001; Maloney and Hartmann 2000), monsoon systems (Pai et al. 2011; Lavender and Matthews 2009), and global weather extremes (Jones et al. 2004). An MJO dependence on SST could also explain features from past warm climates, like the Pliocene “permanent El Niño” (Tziperman and Farrell 2009), and may have caused superrotation during the Eocene (Caballero and Huber 2010).

Acknowledgments. The authors thank Dave Raymond and two anonymous reviewers for their constructive comments. This work was supported by an NSF Graduate Research Fellowship (NA) and NSF Grants AGS-1303604 (NA, ET) and AGS-1062016 (ZK). ET thanks the Weizmann institute for its hospitality during parts of this work. We would like to acknowledge high-performance computing support from Yellowstone provided by NCAR’s Computational and Information Systems Laboratory, sponsored by the National Science Foundation.

REFERENCES

- Adler, R. F., and Coauthors, 2003: The Version-2 Global Precipitation Climatology Project (GPCP) monthly precipitation analysis (1979–present). *J. Hydrometeorol.*, **4**, 1147–1167, doi:10.1175/1525-7541(2003)004<1147:TVGPCP>2.0.CO;2.
- Andersen, J. A., and Z. Kuang, 2012: Moist static energy budget of MJO-like disturbances in the atmosphere of a zonally symmetric aquaplanet. *J. Climate*, **25**, 2782–2804, doi:10.1175/JCLI-D-11-00168.1.
- Aralgidad, N. M., and E. D. Maloney, 2008: Wind-driven latent heat flux and the intraseasonal oscillation. *Geophys. Res. Lett.*, **35**, L04815, doi:10.1029/2007GL032746.
- Arnold, N. P., Z. Kuang, and E. Tziperman, 2013: Enhanced MJO-like variability at high SST. *J. Climate*, **26**, 988–1001, doi:10.1175/JCLI-D-12-00272.1.
- , M. Branson, M. A. Burt, D. S. Abbot, Z. Kuang, D. A. Randall, and E. Tziperman, 2014: The effects of explicit atmospheric convection at high CO₂. *Proc. Natl. Acad. Sci. USA*, **111**, 10943–10948, doi:10.1073/pnas.1407175111.
- Bellon, G., and A. Sobel, 2008: Poleward-propagating intraseasonal monsoon disturbances in an intermediate-complexity axisymmetric model. *J. Atmos. Sci.*, **65**, 470–489, doi:10.1175/2007JAS2339.1.
- Benedict, J. J., and D. A. Randall, 2009: Structure of the Madden-Julian oscillation in the superparameterized CAM. *J. Atmos. Sci.*, **66**, 3277–3296, doi:10.1175/2009JAS3030.1.
- , E. D. Maloney, A. H. Sobel, and D. M. W. Frierson, 2014: Gross moist stability and MJO simulation skill in three full-physics GCMs. *J. Atmos. Sci.*, **71**, 3327–3349, doi:10.1175/JAS-D-13-0240.1.
- Bladé, I., and D. L. Hartmann, 1993: Tropical intraseasonal oscillations in a simple nonlinear model. *J. Atmos. Sci.*, **50**, 2922–2939, doi:10.1175/1520-0469(1993)050<2922:TIOIAS>2.0.CO;2.
- Bretherton, C. S., M. E. Peters, and L. E. Back, 2004: Relationships between water vapor path and precipitation over the tropical oceans. *J. Climate*, **17**, 1517–1528, doi:10.1175/1520-0442(2004)017<1517:RBWVPA>2.0.CO;2.
- Caballero, R., and M. Huber, 2010: Spontaneous transition to superrotation in warm climates simulated by CAM3. *Geophys. Res. Lett.*, **37**, L11701, doi:10.1029/2010GL043468.
- Clement, A. C., R. Seager, M. A. Cane, and S. E. Zebiak, 1996: An ocean dynamical thermostat. *J. Climate*, **9**, 2190–2196, doi:10.1175/1520-0442(1996)009<2190:AODT>2.0.CO;2.
- Derbyshire, S., I. Beau, P. Bechtold, J.-Y. Grandpeix, J.-M. Piriou, J.-L. Redelsperger, and P. Soares, 2004: Sensitivity of moist convection to environmental humidity. *Quart. J. Roy. Meteor. Soc.*, **130**, 3055–3079, doi:10.1256/qj.03.130.
- Dowsett, H. J., A. M. Haywood, P. J. Valdes, M. M. Robinson, D. J. Lunt, D. J. Hill, D. K. Stoll, and K. M. Foley, 2011: Sea surface temperatures of the mid-Piacenzian warm period: A comparison of PRISM3 and HadCM3. *Palaeogeogr. Palaeoclimatol. Palaeoecol.*, **309**, 83–91, doi:10.1016/j.palaeo.2011.03.016.
- Emanuel, K. A., 1987: An air-sea interaction model of intraseasonal oscillations in the tropics. *J. Atmos. Sci.*, **44**, 2324–2340, doi:10.1175/1520-0469(1987)044<2324:AASIMO>2.0.CO;2.
- Fedorov, A. V., C. M. Brierley, K. T. Lawrence, Z. Liu, P. S. Dekens, and A. C. Ravelo, 2013: Patterns and mechanisms of early Pliocene warmth. *Nature*, **496**, 43–52, doi:10.1038/nature12003.
- Frank, W. M., and P. E. Roundy, 2006: The role of tropical waves in tropical cyclogenesis. *Mon. Wea. Rev.*, **134**, 2397–2417, doi:10.1175/MWR3204.1.
- Fuchs, Z., and D. J. Raymond, 2002: Large-scale modes of a non-rotating atmosphere with water vapor and cloud-radiation feedbacks. *J. Atmos. Sci.*, **59**, 1669–1679, doi:10.1175/1520-0469(2002)059<1669:LSMOAN>2.0.CO;2.
- Gill, A. E., 1980: Some simple solutions for heat-induced tropical circulation. *Quart. J. Roy. Meteor. Soc.*, **106**, 447–462, doi:10.1002/qj.49710644905.
- Grabowski, W. W., 2001: Coupling cloud processes with the large-scale dynamics using the cloud-resolving convection parameterization (CRCP). *J. Atmos. Sci.*, **58**, 978–997, doi:10.1175/1520-0469(2001)058<0978:CCPWT>2.0.CO;2.
- , 2003: MJO-like coherent structures: Sensitivity simulations using the cloud-resolving convection parameterization (CRCP). *J. Atmos. Sci.*, **60**, 847–864, doi:10.1175/1520-0469(2003)060<0847:MLCSSS>2.0.CO;2.
- , 2004: An improved framework for superparameterization. *J. Atmos. Sci.*, **61**, 1940–1952, doi:10.1175/1520-0469(2004)061<1940:AIFFS>2.0.CO;2.
- Grodsky, S. A., A. Bentamy, J. A. Carton, and R. T. Pinker, 2009: Intraseasonal latent heat flux based on satellite observations. *J. Climate*, **22**, 4539–4556, doi:10.1175/2009JCLI2901.1.
- Hall, J. D., A. J. Matthews, and D. J. Karoly, 2001: The modulation of tropical cyclone activity in the Australian region by the Madden-Julian oscillation. *Mon. Wea. Rev.*, **129**, 2970–2982, doi:10.1175/1520-0493(2001)129<2970:TMOTCA>2.0.CO;2.
- Held, I. M., and B. J. Soden, 2006: Robust responses of the hydrological cycle to global warming. *J. Climate*, **19**, 5686–5699, doi:10.1175/JCLI3990.1.
- Hendon, H. H., and B. Liebmann, 1990: A composite study of onset of the Australian summer monsoon. *J. Atmos. Sci.*, **47**, 2227–2240, doi:10.1175/1520-0469(1990)047<2227:ACSOOO>2.0.CO;2.
- , C. Zhang, and J. D. Glick, 1999: Interannual variation of the Madden-Julian oscillation during austral summer. *J. Climate*, **12**, 2538–2550, doi:10.1175/1520-0442(1999)012<2538:IVOTMJ>2.0.CO;2.

- , M. C. Wheeler, and C. Zhang, 2007: Seasonal dependence of the MJO–ENSO relationship. *J. Climate*, **20**, 531–543, doi:10.1175/JCLI4003.1.
- Inness, P. M., and J. M. Slingo, 2003: Simulation of the Madden–Julian oscillation in a coupled general circulation model. Part I: Comparison with observations and an atmosphere-only GCM. *J. Climate*, **16**, 345–364, doi:10.1175/1520-0442(2003)016<0345:SOTMJO>2.0.CO;2.
- Jones, C., and L. M. V. Carvalho, 2006: Changes in the activity of the Madden–Julian oscillation during 1958–2004. *J. Climate*, **19**, 6353–6370, doi:10.1175/JCLI3972.1.
- , and —, 2011: Will global warming modify the activity of the Madden–Julian oscillation? *Quart. J. Roy. Meteor. Soc.*, **137**, 544–552, doi:10.1002/qj.765.
- , D. E. Waliser, K. M. Lau, and W. Stern, 2004: Global occurrences of extreme precipitation and the Madden–Julian oscillation: Observations and predictability. *J. Climate*, **17**, 4575–4589, doi:10.1175/3238.1.
- Kalnay, E., and Coauthors, 1996: The NCEP/NCAR 40-Year Reanalysis Project. *Bull. Amer. Meteor. Soc.*, **77**, 437–471, doi:10.1175/1520-0477(1996)077<0437:TNYRP>2.0.CO;2.
- Khairoutdinov, M. F., and D. A. Randall, 2003: Cloud resolving modeling of the ARM summer 1997 IOP: Model formulation, results, uncertainties, and sensitivities. *J. Atmos. Sci.*, **60**, 607–625, doi:10.1175/1520-0469(2003)060<0607:CRMOTA>2.0.CO;2.
- Kim, D., A. H. Sobel, and I.-S. Kang, 2011: A mechanism denial study on the Madden–Julian Oscillation. *J. Adv. Model. Earth Syst.*, **3**, M12007, doi:10.1029/2011MS000081.
- , J.-S. Kug, and A. H. Sobel, 2014: Propagating versus non-propagating Madden–Julian oscillation events. *J. Climate*, **27**, 111–125, doi:10.1175/JCLI-D-13-00084.1.
- Kiranmayi, L., and E. Maloney, 2011: The intraseasonal moist static energy budget in reanalysis data. *J. Geophys. Res.*, **116**, D21117, doi:10.1029/2011JD016031.
- Lavender, S. L., and A. J. Matthews, 2009: Response of the West African monsoon to the Madden–Julian oscillation. *J. Climate*, **22**, 4097–4116, doi:10.1175/2009JCLI2773.1.
- Lawrence, D. M., and P. J. Webster, 2002: The boreal summer intraseasonal oscillation: Relationship between northward and eastward movement of convection. *J. Atmos. Sci.*, **59**, 1593–1606, doi:10.1175/1520-0469(2002)059<1593:TBSIOR>2.0.CO;2.
- Lee, J.-Y., B. Wang, M. C. Wheeler, X. Fu, D. E. Waliser, and I.-S. Kang, 2013: Real-time multivariate indices for the boreal summer intraseasonal oscillation over the Asian summer monsoon region. *Climate Dyn.*, **40**, 493–509, doi:10.1007/s00382-012-1544-4.
- Lee, S., 1999: Why Are the climatological zonal winds easterly in the equatorial upper troposphere? *J. Atmos. Sci.*, **56**, 1353–1363, doi:10.1175/1520-0469(1999)056<1353:WATCZW>2.0.CO;2.
- Liebmann, B., and C. Smith, 1996: Description of a complete (interpolated) outgoing longwave radiation dataset. *Bull. Amer. Meteor. Soc.*, **77**, 1275–1277.
- , H. Hendon, and J. Glick, 1994: The relationship between tropical cyclones of the western Pacific and Indian Oceans and the Madden–Julian oscillation. *J. Meteor. Soc. Japan*, **72**, 401–412.
- Lin, J., B. Mapes, M. Zhang, and M. Newman, 2004: Stratiform precipitation, vertical heating profiles, and the Madden–Julian oscillation. *J. Atmos. Sci.*, **61**, 296–309, doi:10.1175/1520-0469(2004)061<0296:SPVHPA>2.0.CO;2.
- , G. N. Kiladis, B. E. Mapes, K. M. Weickmann, K. R. Sperber, W. Lin, M. C. Wheeler, and S. D. Schubert, 2006: Tropical intraseasonal variability in 14 IPCC AR4 climate models. Part I: Convective signals. *J. Climate*, **19**, 2665–2690, doi:10.1175/JCLI3735.1.
- Liu, P., T. Li, B. Wang, M. Zhang, J.-J. Luo, Y. Masumoto, X. Wang, and E. Roeckner, 2013: MJO change with A1B global warming estimated by the 40-km ECHAM5. *Climate Dyn.*, **41**, 1009–1023, doi:10.1007/s00382-012-1532-8.
- Madden, R. A., and P. R. Julian, 1971: Detection of a 40–50 day oscillation in the zonal wind in the tropical Pacific. *J. Atmos. Sci.*, **28**, 702–708, doi:10.1175/1520-0469(1971)028<0702:DOADOI>2.0.CO;2.
- Maloney, E. D., 2002: An intraseasonal oscillation composite life cycle in the NCAR CCM3.6 with modified convection. *J. Climate*, **15**, 964–982, doi:10.1175/1520-0442(2002)015<0964:AIOCLC>2.0.CO;2.
- , 2009: The moist static energy budget of a composite tropical intraseasonal oscillation in a climate model. *J. Climate*, **22**, 711–729, doi:10.1175/2008JCLI2542.1.
- , and D. L. Hartmann, 2000: Modulation of eastern North Pacific hurricanes by the Madden–Julian oscillation. *J. Climate*, **13**, 1451–1460, doi:10.1175/1520-0442(2000)013<1451:MOENPH>2.0.CO;2.
- , and A. H. Sobel, 2004: Surface fluxes and ocean coupling the tropical intraseasonal oscillation. *J. Climate*, **17**, 4368–4386, doi:10.1175/JCLI-3212.1.
- , and S.-P. Xie, 2013: Sensitivity of tropical intraseasonal variability to the pattern of climate warming. *J. Adv. Model. Earth Syst.*, **5**, 32–47, doi:10.1029/2012MS000171.
- , A. H. Sobel, and W. M. Hannah, 2010: Intraseasonal variability in an aquaplanet general circulation model. *J. Adv. Model. Earth Syst.*, **2**, doi:10.3894/JAMES.2010.2.5.
- Matsuno, T., 1966: Quasi-geostrophic motions in the equatorial area. *J. Meteor. Soc. Japan*, **44**, 25–42.
- Matthews, A. J., B. J. Hoskins, and M. Masutani, 2004: The global response to tropical heating in the Madden–Julian oscillation during northern winter. *Quart. J. Roy. Meteor. Soc.*, **130**, 1991–2011, doi:10.1256/qj.02.123.
- McPhaden, M. J., 1999: Genesis and evolution of the 1997–98 El Niño. *Science*, **283**, 950–954, doi:10.1126/science.283.5404.950.
- Neale, R. B., J. H. Richter, and M. Jochum, 2008: The impact of convection on ENSO: From a delayed oscillator to a series of events. *J. Climate*, **21**, 5904–5924, doi:10.1175/2008JCLI2244.1.
- Neelin, J. D., I. M. Held, and K. H. Cook, 1987: Evaporation–wind feedback and low-frequency variability in the tropical atmosphere. *J. Atmos. Sci.*, **44**, 2341–2348, doi:10.1175/1520-0469(1987)044<2341:EWFAF>2.0.CO;2.
- Oliver, E. C., and K. R. Thompson, 2012: A reconstruction of Madden–Julian oscillation variability from 1905 to 2008. *J. Climate*, **25**, 1996–2019, doi:10.1175/JCLI-D-11-00154.1.
- Pai, D. S., J. Bhate, O. P. Sreejith, and H. R. Hatwar, 2011: Impact of MJO on the intraseasonal variation of summer monsoon rainfall over India. *Climate Dyn.*, **36**, 41–55, doi:10.1007/s00382-009-0634-4.
- Pritchard, M. S., and R. C. J. Somerville, 2009: Assessing the diurnal cycle of precipitation in a multi-scale climate model. *J. Adv. Model. Earth Syst.*, **1**, doi:10.3894/JAMES.2009.1.12.
- , and C. S. Bretherton, 2014: Causal evidence that rotational moisture advection is critical to the superparameterized Madden–Julian oscillation. *J. Atmos. Sci.*, **71**, 800–815, doi:10.1175/JAS-D-13-0119.1.
- Randall, D., M. Khairoutdinov, A. Arakawa, and W. Grabowski, 2003: Breaking the cloud parameterization deadlock. *Bull. Amer. Meteor. Soc.*, **84**, 1547–1564, doi:10.1175/BAMS-84-11-1547.
- Raymond, D. J., and Z. Fuchs, 2009: Moisture modes and the Madden–Julian oscillation. *J. Climate*, **22**, 3031–3046, doi:10.1175/2008JCLI2739.1.

- Reynolds, R., N. Rayner, T. Smith, D. Stokes, and W. Wang, 2002: An improved in situ and satellite SST analysis for climate. *J. Climate*, **15**, 1609–1625, doi:10.1175/1520-0442(2002)015<1609:AIISAS>2.0.CO;2.
- Schubert, J. J., B. Stevens, and T. Crueger, 2013: Madden-Julian oscillation as simulated by the MPI Earth System Model: Over the last and into the next millennium. *J. Adv. Model. Earth Syst.*, **5**, 71–84, doi:10.1029/2012MS000180.
- Slingo, J. M., D. P. Rowell, K. R. Sperber, and F. Nortley, 1999: On the predictability of the interannual behaviour of the Madden-Julian oscillation and its relationship with El Niño. *Quart. J. Roy. Meteor. Soc.*, **125**, 583–609, doi:10.1002/qj.49712555411.
- Sobel, A., and E. Maloney, 2012: An idealized semi-empirical framework for modeling the Madden-Julian oscillation. *J. Atmos. Sci.*, **69**, 1691–1705, doi:10.1175/JAS-D-11-0118.1.
- , J. Nilsson, and L. M. Polvani, 2001: The weak temperature gradient approximation and balanced tropical moisture waves. *J. Atmos. Sci.*, **58**, 3650–3665, doi:10.1175/1520-0469(2001)058<3650:TWTGAA>2.0.CO;2.
- , E. D. Maloney, G. Bellon, and D. M. Frierson, 2010: Surface fluxes and tropical intraseasonal variability: A reassessment. *J. Adv. Model. Earth Syst.*, **2** (2), doi:10.3894/JAMES.2010.2.2.
- Stan, C., M. Khairoutdinov, C. A. DeMott, V. Krishnamurthy, D. M. Straus, D. A. Randall, I. J. L. Kinter, and J. Shukla, 2010: An ocean-atmosphere climate simulation with an embedded cloud resolving model. *Geophys. Res. Lett.*, **37**, L01702, doi:10.1029/2009GL040822.
- Stocker, T. F., and Coauthors, 2014: Technical summary. *Climate Change 2013: The Physical Science Basis*, T. F. Stocker et al., Eds., Cambridge University Press, 33–115.
- Subramanian, A., M. Jochum, A. J. Miller, R. Neale, H. Seo, D. Waliser, and R. Murtugudde, 2014: The MJO and global warming: A study in CCSM4. *Climate Dyn.*, **42**, 2019–2031, doi:10.1007/s00382-013-1846-1.
- Takahashi, C., N. Sato, A. Seiki, K. Yoneyama, and R. Shirooka, 2011: Projected future change of MJO and its extratropical teleconnection in East Asia during the northern winter simulated in IPCC AR4 models. *SOLA*, **7**, 201–204, doi:10.2151/sola.2011-051.
- Thayer-Calder, K., and D. A. Randall, 2009: The role of convective moistening in the Madden-Julian oscillation. *J. Atmos. Sci.*, **66**, 3297–3312, doi:10.1175/2009JAS3081.1.
- Tziperman, E., and B. Farrell, 2009: Pliocene equatorial temperature: Lessons from atmospheric superrotation. *Paleoceanography*, **24**, PA1101, doi:10.1029/2008PA001652.
- Wara, M. W., A. C. Ravelo, and M. L. Delaney, 2005: Permanent El Niño-like conditions during the Pliocene warm period. *Science*, **309**, 758–762, doi:10.1126/science.1112596.
- Wheeler, M. C., and G. N. Kiladis, 1999: Convectively coupled equatorial waves: Analysis of clouds and temperature in the wavenumber–frequency domain. *J. Atmos. Sci.*, **56**, 374–399, doi:10.1175/1520-0469(1999)056<0374:CCEWAO>2.0.CO;2.
- , and H. H. Hendon, 2004: An all-season real-time multivariate MJO index: Development of an index for monitoring and prediction. *Mon. Wea. Rev.*, **132**, 1917–1932, doi:10.1175/1520-0493(2004)132<1917:AARMMI>2.0.CO;2.
- Yamaguchi, K., and A. Noda, 2006: Global warming patterns over the North Pacific: ENSO vs AO. *J. Meteor. Soc. Japan*, **84**, 221–241, doi:10.2151/jmsj.84.221.
- Zhang, C., 2005: Madden-Julian oscillation. *Rev. Geophys.*, **43**, RG2003, doi:10.1029/2004RG000158.
- , and M. Dong, 2004: Seasonality in the Madden-Julian oscillation. *J. Climate*, **17**, 3169–3180, doi:10.1175/1520-0442(2004)017<3169:SITMO>2.0.CO;2.
- , —, S. Gualdi, H. H. Hendon, E. D. Maloney, A. Marshall, K. R. Sperber, and W. Wang, 2006: Simulations of the Madden-Julian oscillation in four pairs of coupled and uncoupled global models. *Climate Dyn.*, **27**, 573–592, doi:10.1007/s00382-006-0148-2.
- Zhang, Y. G., M. Pagani, and Z. Liu, 2014: A 12-million-year temperature history of the tropical Pacific Ocean. *Science*, **344**, 84–87, doi:10.1126/science.1246172.